

Local ferroelectric polarization in antiferroelectric chalcogenide perovskite BaZrS₃ thin filmsJuhi Pandey ¹, Debjit Ghoshal,² Dibyendu Dey ^{3,4}, Tushar Gupta ⁵, A. Taraphder ³, Nikhil Koratkar ⁵ and Ajay Soni ^{1,*}¹*School of Basic Sciences, Indian Institute of Technology Mandi, Mandi 175075, Himachal Pradesh, India*²*Department of Chemical and Biological Engineering, Rensselaer Polytechnic Institute, Troy, New York 12180, USA*³*Department of Physics and Centre for Theoretical Studies, Indian Institute of Technology Kharagpur, Kharagpur 721302, India*⁴*Department of Physics, Arizona State University, Tempe, Arizona 85287, USA*⁵*Department of Mechanical, Aerospace and Nuclear Engineering, Rensselaer Polytechnic Institute, Troy, New York 12180, USA*

(Received 18 September 2020; accepted 3 November 2020; published 30 November 2020)

Bulk chalcogenide perovskite BaZrS₃ (BZS), with a direct band gap in the visible region, is an important photovoltaic material, albeit with limited applicability owing to its antiferroelectric (AF) nature. Presently, ferroelectric (FE) perovskite-based photovoltaics are attracting enormous attention for environmental stability and better energy conversion efficiency through enhanced charge separation. We report on AF-FE phases of BZS thin film using temperature-dependent Raman investigations and first-principles calculations. Origin of localized FE phase is established from an anomalous behavior of $A_g^7 \sim 300 \text{ cm}^{-1}$ and $B_{1g}^5 \sim 420 \text{ cm}^{-1}$ modes, which involve the vibration of atoms at the apical site of ZrS₆ octahedra. Additionally, B_{1g}^1 and B_{2g}^2 ($\sim 85 \text{ cm}^{-1}$) modes appear while antipolar B_{2g}^1 ($\sim 60 \text{ cm}^{-1}$) disappears below 60 K. Our first-principles calculations confirm that FE appears as a result of the loss of center of inversion symmetry in ZrS₆ due to the existence of oxygen impurities placed locally at apical sites of sulfur.

DOI: [10.1103/PhysRevB.102.205308](https://doi.org/10.1103/PhysRevB.102.205308)**I. INTRODUCTION**

Perovskite materials have remarkable technological importance in the field of photovoltaics, optoelectronics, energy harvesting, ferroelectricity, electrocatalysis, photocatalysis, magnetic storage, and spintronics because of their exotic optical, mechanical, magnetic, and electrical transport properties [1–5]. Several transition metal chalcogenide perovskites (TMCPs), such as CaZrS₃, BaZrS₃, SrZrS₃, have emerged as nontoxic and environmentally stable photovoltaic material with an electronic band gap in the visible region [1,3,6,7]. Further, to achieve optimum photovoltaic performance, the electronic band gap can be modulated by alloying and doping. Commonly, TMCPs are distorted perovskites with either antiferroelectric (AF) or paraelectric (PE) properties. Therefore, engineering ferroelectricity by designing nanoscale materials is necessary to develop promising ferroelectric (FE) TMCPs. Noticeably, there are several ways to induce the AF-FE phase in AF materials owing to comparable energy of AF and FE phases [8]. Thin films of AF materials below a critical thickness induces the FE phase due to a surface effect, epitaxial strain, and dimensionality of nanostructures [8]. For instance, bulk PbZrO₃ is AF in nature but single-crystalline films below $\sim 22 \text{ nm}$ thickness have demonstrated FE phases due to epitaxial strain [9]. Additionally, FE phases in thin films can also be induced by the application of a large electric field which generally results in large lattice strain and high electrostatic energy density. Thus, the pairing of epitaxial thin film of FE and AF materials is gaining in-

creasing attention for integration into standard semiconductor technology [10].

Bulk BaZrS₃ (BZS) is an AF chalcogenide perovskite having a direct band gap in the range of 1.7–1.85 eV and has strong absorption in the visible spectrum [3]. The band gap in BZS can be tuned by cation or anion alloying, and fractional substitution of Zr atoms for possible application in single junction solar cell [11]. Bulk BZS shows long term stability against environmental conditions at low temperature and high pressure, in contrast to oxides having very high band gap and alternative-halide perovskites which are unstable against surface oxidation and moisture [7,12,13]. Additionally, thin films of BZS can show FE phases and modified functional properties due to strain, lattice mismatch with a substrate, impurities, defects, and superlattice formation. In this regard, unlike the established understanding of phase transition in bulk TMCPs, thin films of perovskites are not yet well explored and tuning of FE-AF-PE nature by replacement of atoms at anion site for TMCPs is an open challenge.

In the present study, we report a systematic study of AF-FE nanoscale phases, in chemical vapor deposition (CVD) grown BZS thin film, using temperature-dependent Raman investigation, optical spectroscopy, and first-principles calculations. We have investigated the ferroic nature and the origin of AF to FE transition by analyzing the anomalous behavior of four Raman modes and appearances of a new mode, which are important for understanding the structural stability of BZS and ferroic polarizations, especially at the nanoscale. The outcome highlights the feasibility of achieving local FE phases in a thin film of BZS, which can show optoelectronic properties superior than the bulk AF-BZS as advanced photovoltaic materials.

*Corresponding author: ajay@iitmandi.ac.in

II. EXPERIMENT

A. Sample preparation and characterizations

The thin film of BZS was grown over quartz substrate by the CVD technique. In the process, a predeposited BaZrO₃ film over quartz substrate was treated with a mixture of N₂ and CS₂ vapors for sulfurization, which resulted in continuous BZS film. Details of the CVD process and the growth parameters were described in earlier work. The thickness of the film was found to be ~ 230 nm [7]. An optical image of the BZS thin film was obtained using an Olympus BX53 microscope with 100 \times objective and the morphology was characterized by JFEI, Nova Nano SEM-450, field emission scanning electron microscopy (FESEM) at 15 kV acceleration voltage. Elemental composition of the film was mapped by energy dispersive spectroscopy (EDS) coupled with FESEM. To assess the crystal structure and phase purity, XRD was done using rotating anode Rigaku Smartlab diffractometer in Bragg-Brentano geometry with Cu-K α radiation ($\lambda = 1.5406$ Å). Micro-Raman measurements were performed using a Horiba Jobin-Yvon LabRAM HR evolution Raman spectrometer in backscattering geometry with He-Ne laser excitation ~ 633 nm (for near resonant Raman) and solid-state laser excitation ~ 785 nm (for nonresonant Raman), 1800 gr/mm grating and a Peltier cooled charge-coupled device detector. A micro-Photoluminescence study was performed using the same Raman spectrometer with 532 nm (2.3 eV) laser excitation and 600 gr/mm grating. Temperature-dependent Raman and PL were performed using a Montana cryostat in the range of 3–300 K. The optical band gap of the film was estimated using a Perkin Elmer UV/Vis/NIR spectrometer Lambda 750 at room temperature in absorbance mode. X-ray photoelectron spectroscopy (XPS) measurements were performed to determine the elemental composition and the chemical state by using a Nexsa instrument (Thermo Fisher Scientific) having Al-K α as the x-ray source.

B. Computational details

First-principles calculations, based on density functional theory (DFT) [14,15], were performed by using a plane-wave basis set and projector-augmented wave (PAW) potentials [16,17], as implemented in the Vienna *ab-initio* simulation package (VASP) [18]. The wave functions were expanded in the plane-wave basis with a kinetic-energy cutoff of 500 eV. For the exchange-correlation function, we used the generalized gradient approximation (GGA) with the Perdew-Burke-Ernzerhof (PBE) functional [19]. The reciprocal space integration was carried out with a Γ -centered k mesh of $8 \times 6 \times 8$. During structural relaxations, positions of the ions were relaxed until the Hellman-Feynman forces became less than 10^{-3} eV/Å. Phonons were calculated from density functional perturbation theory (DFPT) as implemented in the PHONOPY code [20]. The macroscopic electronic polarization has been calculated by using the Berry phase expressions [21].

III. RESULT AND DISCUSSION

Surface morphology in optical image [Fig. 1(a)] and SEM micrograph [Fig. 1(b)] depicts the polycrystalline nature of the

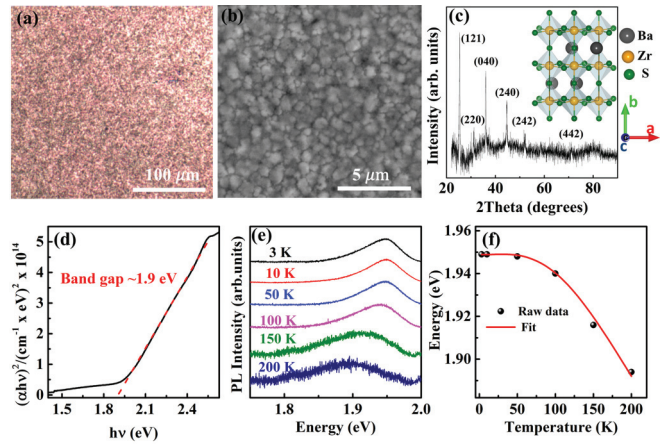


FIG. 1. (a) Optical image and (b) SEM micrograph, and (c) XRD pattern of CVD grown BZS thin film on quartz substrate, inset showing distorted orthorhombic unit cell with $Pnma$ (D_{2h}^{16}) space group. (d) Absorbance spectra at 300 K with extrapolated dashed red line showing a direct band gap (~ 1.9 eV), (e) temperature dependent PL spectra, and (f) energy vs temperature graph; the red line presents hyperbolic cotangent fitting of redshift of PL peak position, which estimates the band gap ~ 1.95 eV at 0 K.

BZS thin film. Phase purity and crystallinity of BZS film are determined by an x-ray diffraction (XRD) pattern [Fig. 1(c)] and the peak positions are matched with JCPDS card no. 00-015-0327. Estimated lattice parameters are $a = 6.984$ Å, $b = 9.956$ Å, and $c = 6.934$ Å, which are slightly smaller than the bulk lattice parameters $a = 7.061$ Å, $b = 9.977$ Å, and $c = 7.014$ Å, possibly due to substrate driven strain in the film [6]. The analysis of XRD pattern shows that the film is grown with distorted perovskite orthorhombic crystal structure [space group $Pnma$ (D_{2h}^{16})], shown in the inset of Fig. 1(c). The Wyckoff positions of various atoms are Ba at $4(c) : x, \frac{1}{4}, z$; Zr at $4(b) : 0, 0, \frac{1}{2}$; and the first sulfur atom S^I at $4(c)$ and second sulfur atom S^{II} at $8(d) : x, y, z$. A careful examination of the crystal structure suggests that the unit cell for the BZS perovskite contains a network of distorted corner sharing ZrS₆ octahedra with Zr atoms placed at the center of each octahedron. Here, Ba atoms are caged centrally between the networks of neighboring ZrS₆ units. The octahedral rotations and expansions along with antipolar displacement of the Ba site from ideal perovskite structure (tolerance factor $t = 1$; the details of t are given in the Supplemental Material [22]) [23–26] often suppress ferroelectricity in perovskites with $Pnma$ structure [25]. Overlay image and elemental mapping for Ba, Zr, and S atoms confirm the uniform and stoichiometric distribution of atoms in the film (Fig. S1 of the Supplemental Material [22]). The estimated ratio of Ba:Zr:S atoms is found to be 1:1.2:3.3, which is consistent with the chemical formula of BZS.

Optical properties of the BZS film have been characterized using absorbance and temperature-dependent PL measurements. Figure 1(d) shows the absorption spectrum of the film, where α is the absorption coefficient and $h\nu$ represents the energy of incident light. The linear dependence of the $(\alpha h\nu)^2$ vs $h\nu$ plot near the band edge confirms that the BZS thin film is a direct band gap (~ 1.9 eV) material, at room temperature.

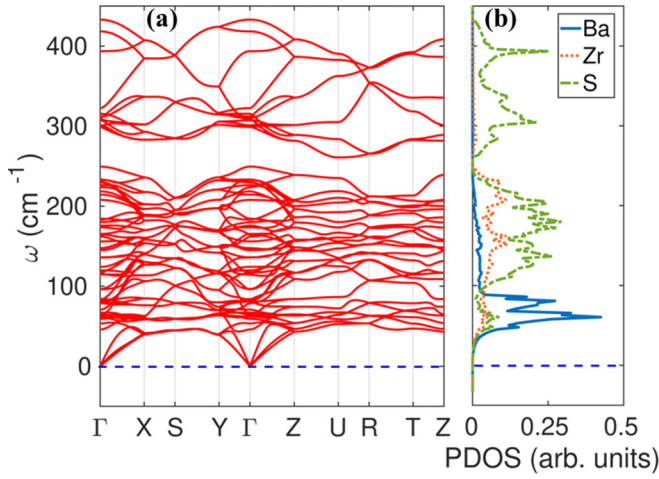


FIG. 2. (a) Phonon dispersion of BZS film and (b) atom-projected phonon DOS for Ba, Zr, and S atoms.

Normalized PL spectra [Fig. 1(e)] show a single broad asymmetric emission peak with the band gap varying from ~ 1.95 to ~ 1.85 eV with the rise in temperature. The variation of optical band gap with temperature [Fig. 1(f)] is fitted with the standard hyperbolic cotangent, $E(T) = E(0) - C \times E_{\text{ph}} [\coth(\frac{E_{\text{ph}}}{k_B T}) - 1]$, where $E(0)$ is the optical band gap at 0 K, C is a dimensionless electron-phonon coupling constant, k_B is

Boltzmann's constant, and E_{ph} is the average phonon energy coupling to the electron [27]. Here, the redshift of the optical band gap is related to electron-phonon coupling and the estimated $E(0)$ is found to be ~ 1.95 eV and $E_{\text{ph}} = 14.8$ meV (~ 120 cm^{-1}) for the BZS thin films.

To understand the effect of strain on the vibrational properties of BZS film, we have generated phonon band structure and phonon density of states (PDOS) from its experimental lattice parameters (Fig. 2). The $Pnma$ (D_{2h}^{16}) structure of BZS contains four formula units per unit cell resulting in 57 zone-center optical phonons classified as $(7A_g + 5B_{1g} + 7B_{2g} + 5B_{3g}) + (9B_{1u} + 7B_{2u} + 9B_{3u}) + 8A_u$, where only the first 24 are Raman active. The next set of 25 modes are infrared active whereas the eight A_u modes are optically inactive [28]. Calculated Raman-active modes, consistent with the earlier work by Gross *et al.* [12], are presented in Table S1 in the Supplemental Material [22]. The dynamical stability of the compound is manifested through the absence of imaginary modes in the phonon band structure [Fig. 2(a)]. Atom-projected PDOS reveals that the low-frequency modes (< 100 cm^{-1}) have main contributions coming from the vibration of the Ba atoms while the high-frequency modes (> 250 cm^{-1}) are dominated by the atomic vibration of the S atoms. However, the midfrequency phonons involve the vibration of both Zr and S atoms.

The Raman spectra at 10 K are quite distinct from the spectra at 260 K [Fig. 3(a)], due to reduced spectral width at low temperature and the appearance of new modes. Since

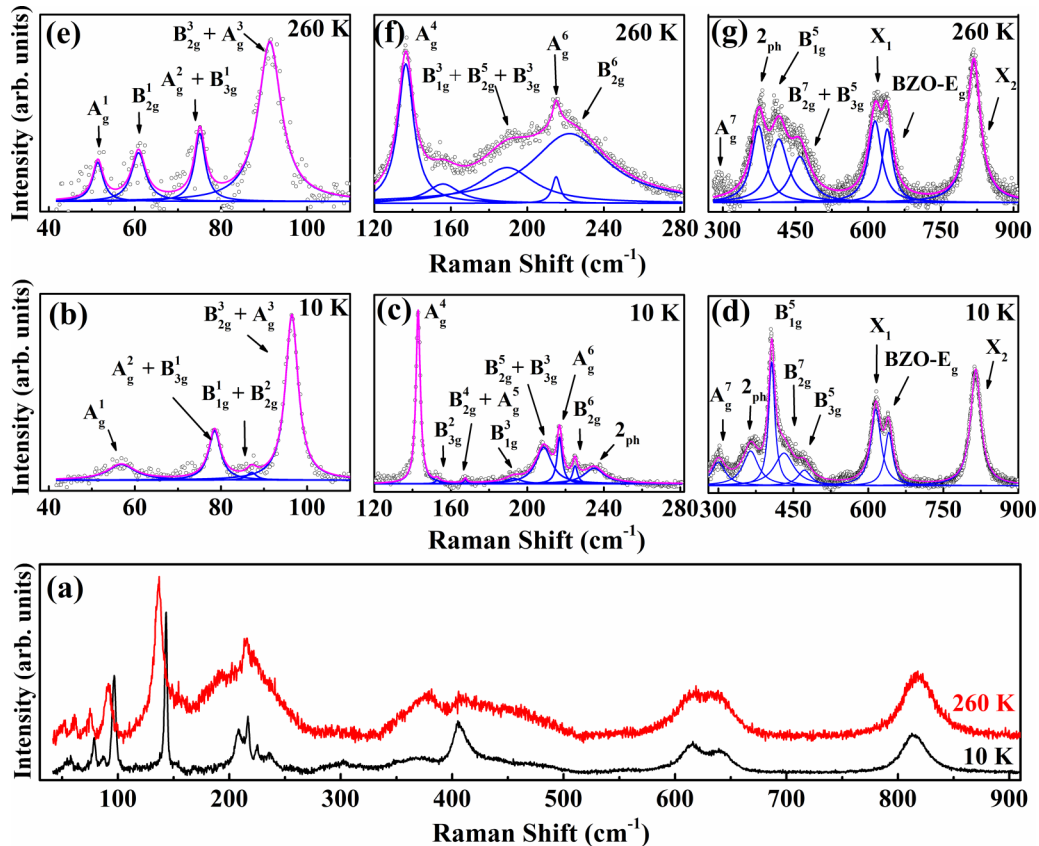


FIG. 3. Raman spectrum of BZS thin film showing (a) comparison of spectra at 10 and 260 K, and Lorentzian fitting of the Raman spectra for the spectral range (b),(e) 40–120 cm^{-1} , (c),(f) 120–280 cm^{-1} , and (d),(g) 300–900 cm^{-1} at 10 and 260 K, respectively. Open circles represent raw data, blue solid lines correspond to best-fit results of the individual peak, and pink curve shows the cumulative spectrum.

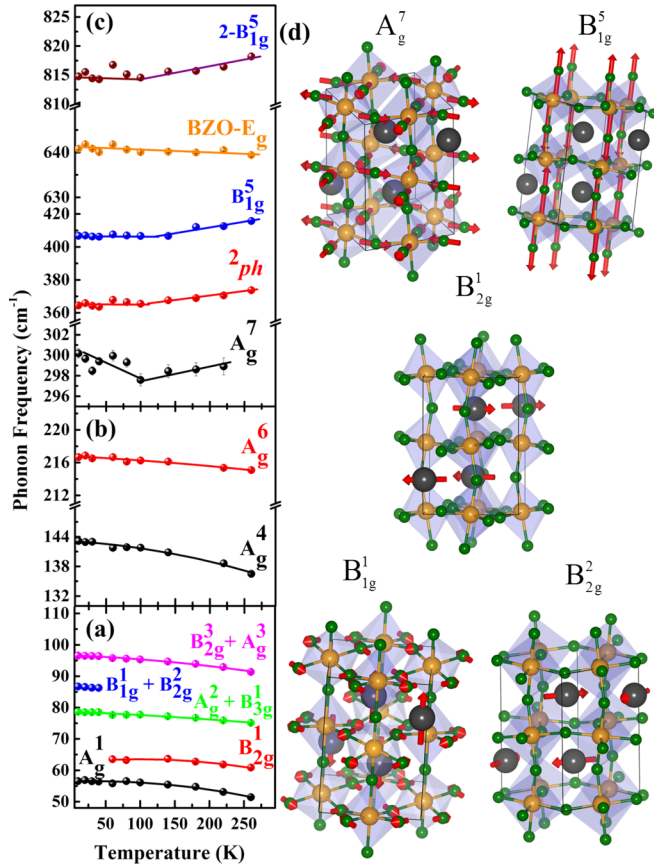


FIG. 4. Temperature dependence of phonon frequency for the spectral range (a) 40–120 cm^{-1} , (b) 120–280 cm^{-1} , (c) 280–830 cm^{-1} , (d) schematic of the five Raman-active modes having anomalous response with temperature.

the 300-K Raman spectra are little noisy (Fig. S2 of the Supplemental Material [22]), we have chosen the 260-K data. Figures 3(b)–3(d) show the detailed spectra of 10 K, while Figs. 3(e)–3(g) show the spectra for 260 K in three spectral ranges: (i) 40–120 cm^{-1} , (ii) 120–280 cm^{-1} , and (iii) 300–900 cm^{-1} , respectively. Each spectral range is fitted with a multiple Lorentzian peak function to estimate peak position and the origin of the peaks has been assigned (tabulated in the Supplemental Material, Table S1 [22]), according to our phonon calculations shown in Fig. 2.

Temperature dependence of phonon frequency is presented in Fig. 4, while the complete spectrum is shown in Fig. S2 of the Supplemental Material [22]. All the Raman modes in the spectral range 40–280 cm^{-1} [shown in Figs. 4(a) and 4(b)] are redshifted due to thermal expansion and the corresponding increase in force constant as temperature rises. The reduction in phonon frequency with increasing temperature owes to two major reasons, (i) volume change due to thermal expansion, and (ii) decay of harmonic mode because of multiphonon interactions [29]. To estimate the thermal renormalization of the phonon frequency, the obtained frequency is fitted by the equation $\omega(T) = \omega_0 - A[1 + \frac{2}{(e^x - 1)}] - B[1 + \frac{3}{(e^y - 1)} + \frac{3}{(e^y - 1)^2}]$, where $x = \frac{\hbar\omega_0}{2k_B T}$ and $y = \frac{\hbar\omega_0}{3k_B T}$, ω_0 is the harmonic frequency at $T = 0\text{ K}$, and A and B are anharmonic fitting parameters related to the probability of three-

and four-phonon decay processes [29]. Since the expression of multiphonon decay could not be fitted with the two-phonon process, we have used the three- and four-phonon terms in the expression. Table S2 in the Supplemental Material gives details of the fitting parameters of the corresponding modes [22]. Interestingly, for bulk BZS, B_{2g}^1 ($\sim 60.8\text{ cm}^{-1}$) is prominently present up to 14 K [12], however for the thin film discussed here, this mode appears above 60 K where B_{1g}^1 and B_{2g}^2 ($\sim 85\text{ cm}^{-1}$) disappear. Generally, such emergence and suppression of Raman modes for perovskites signify either modulation in crystal structure or transitions like AF-FE or FE-PE [30,31]. The signature of AFE-FE transition in perovskites is manifested by (a) rearrangement of A site cation, (b) reorientation or tilting of BX_6 octahedra, and (c) off centering of the B-site cation [25,30]. Therefore for AFE-FE transition, major changes in the low-frequency modes representing translational motion of the A-site cation is expected. Here, all the three modes, B_{1g}^1 , B_{2g}^2 , and B_{2g}^1 , involve vibrations of Ba atoms in an antipolar manner with the B_{1g}^1 mode has the rotation of octahedra involved as well. A schematic of atomic vibration for anomalous modes is shown in Fig. 4(d). For perovskites belonging to the nonpolar space group ($Pnma$), the octahedral distortion is considered as the driving mechanism to suppress ferroelectricity by inducing antipolar displacement of Ba-site cations [25]. If Ba-site distortion is not present then octahedral rotations alone will not be able to stabilize the $Pnma$ structure and the system will adopt the $R3c$ structure, which subsequently may develop FE phases [25]. Here, the complete suppression of B_{2g}^1 as well as the reduced Raman intensity of the antipolar A_g^1 mode below 60 K suggest the appearance of FE phases. For perovskites with $t < 1$, the octahedral rotation of ZrS_6 units plays a significant role in AF or FE polarization. Therefore, the cause of transitions can be determined by carefully analyzing the nature of Raman modes involved. While most of the modes have shown the usual redshift of the frequency with increase in temperature, the modes $A_g^7 \sim 300\text{ cm}^{-1}$, $2_{ph} \sim 373\text{ cm}^{-1}$, $B_{1g}^5 \sim 415\text{ cm}^{-1}$, and $X_2 \sim 818\text{ cm}^{-1}$ have shown anomalous behavior [Fig. 4(c)]. Here, the origin of FE transition is established from an anomalous behavior of the A_g^7 mode ($\sim 300\text{ cm}^{-1}$), which involves in-phase stretching of the basal S atom, and the B_{1g}^5 mode ($\sim 420\text{ cm}^{-1}$), which involves out-of-phase stretching of the S atom at the apical site of ZrS_6 octahedra [shown in Fig. 4(d)]. The modes at $\sim 234.9\text{ cm}^{-1}$ and $\sim 365\text{ cm}^{-1}$ are related to two-phonon features (2ph) as observed by Gross *et al.* [12] also. Based on the frequency of $X_2 \sim 818\text{ cm}^{-1}$, which is almost twice $B_{1g}^5 \sim 415\text{ cm}^{-1}$ and shows identical anomalous behavior, we assign this mode to the second order of the B_{1g}^5 mode ($2 - B_{1g}^5$) (Sec. 5 of the Supplemental Material [22]) [32,33]. In addition to these observations, the presence of oxygen (O) impurities due to incomplete sulfurization of the precursor $BaZrO_3$ can result in the localized dipole moment by breaking the center of inversion symmetry of the ZrS_6 octahedra [34]. Since the mode at $\sim 641\text{ cm}^{-1}$ has overlap with the frequency of the E_g mode of $BaZrO_3$, this mode has been assigned as the impurity related mode in BZS [35]. The presence of oxygen impurities reacting with Zr cations is observed in the XPS spectra of the BZS film as discussed in

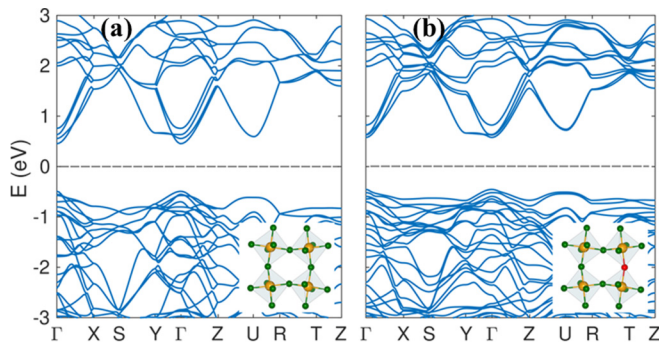


FIG. 5. Electronic band structure of (a) thin-film BZS, and (b) O-BZS with a single O impurity (shown in red color) placed at the apical position of S atom (green color) in ZrS_6 octahedra.

detail in Sec. 6 of the Supplemental Material [22]. From the anomalous behavior of A_g^7 and B_{1g}^5 , one may infer the presence of O impurity in the BZS film coupled with AF-FE transitions.

To understand the role of O impurities in BZS thin film, we have calculated the electronic band structure of pure BZS and O-BZS (O atoms displayed with a red sphere), shown in Fig. 5. The crystal structures of pure BZS and O-BZS with O atom at the single apical site of S atom are shown in the inset of Figs. 5(a) and 5(b), respectively. The electronic band structure of pure BZS [Fig. 5(a)] shows that the material is a semiconductor with a direct band gap ~ 0.95 eV. Since the DFT calculations underestimate the band gap thus the band gap value obtained within GGA is reasonable with the experimental observations. Further, even with the presence of O impurities, the material remains a direct band-gap semiconductor with band-gap value ~ 1.03 eV as shown in Fig. 5(b). Interestingly, our BZS film has a band gap ~ 1.9 eV which is slightly higher than the band gap of bulk BZS ~ 1.85 eV [6], possibly due to the localized O impurities. Our experimental and theoretical studies show that localized O impurities do not modulate the electronic properties of BZS dramatically. We have also investigated the role of any S vacancy that can develop ferroelectricity in BZS. Interestingly, our calculations suggest that the presence of S vacancy modulates electronic band structure and develops metallicity in BZS (shown in

Fig. S5 of the Supplemental Material [22]). Moreover, since pure BZS is AF due to the presence of a center of inversion, we have calculated macroscopic polarization to investigate the ferroic nature of pure-BZS and O-BZS. Our calculations suggest that pristine BZS is AF as $|P| = 0$, whereas O-BZS loses the center of inversion symmetry and develops a net FE polarization with $|P| = 0.26 \mu\text{C}/\text{cm}^2$. To get the exact value of polarization in these thin films, further experiments are required. Several TMCPs such as $\text{Ca}_3\text{Zr}_2\text{S}_7$ and $\text{Ca}_3\text{Hf}_2\text{S}_7$ have high FE polarization, however, the high band gaps of such compounds make them unsuitable for photovoltaic application [36]. On the contrary, chalcogenide perovskites having FE domains along with optimum optical band gap provide an additional route for reduced charge recombination and improved charge transport leading to an efficient photovoltaic application. Thus, our experimental findings supported by theoretical calculations reveal the possible mechanism behind nanoscale FE response in AF-BZS thin film.

IV. CONCLUSION

In summary, we have shown localized FE phases arising from the loss of center of inversion symmetry in AF BZS thin film at nanoscale. The local FE is implied by the anomalous softening of high-frequency Raman-active modes $A_g^7 \sim 300 \text{ cm}^{-1}$ and $B_{1g}^5 \sim 420 \text{ cm}^{-1}$ involving the vibration of S atoms of the ZrS_6 octahedra. The absence of imaginary modes in our phonon band structure confirms that the BZS thin film has dynamically stable $Pnma$ structure. Further, O impurities give local FE but do not modulate the nature and magnitude of the electronic band gap. For pristine BZS, there is no macroscopic electronic polarization ($|P| = 0$), whereas BZS with O impurity has $|P| = 0.26 \mu\text{C}/\text{cm}^2$, implying the localized FE nature of the thin film, thus making it a promising FE photovoltaic material.

ACKNOWLEDGMENTS

A.S. acknowledges Department of Science and Technology, Science and Engineering Research Board, India (Grant No. CRG/2018/002197) for funding support and IIT Mandi for research facilities. N.K. acknowledges funding support from the USA NSF (Award No. 2013640).

- [1] Y.-Y. Sun, M. L. Agiorgousis, P. Zhang, and S. Zhang, *Nano Lett.* **15**, 581 (2015).
- [2] S. Y. Yang, J. Seidel, S. J. Byrnes, P. Shafer, C. H. Yang, M. D. Rossell, P. Yu, Y. H. Chu, J. F. Scott, J. W. Ager III, L. W. Martin, and R. Ramesh, *Nat. Nanotechnol.* **5**, 143 (2010).
- [3] S. Perera, H. Hui, C. Zhao, H. Xue, F. Sun, C. Deng, N. Gross, C. Milleville, X. Xu, D. F. Watson, B. Weinstein, Y.-Y. Sun, S. Zhang, and H. Zeng, *Nano Energy* **22**, 129 (2016).
- [4] M. Li, M. J. Pietrowski, R. A. De Souza, H. Zhang, I. M. Reaney, S. N. Cook, J. A. Kilner, and D. C. Sinclair, *Nat. Mater.* **13**, 31 (2013).
- [5] P.-F. Li, W.-Q. Liao, Y.-Y. Tang, H.-Y. Ye, Y. Zhang, and R.-G. Xiong, *J. Am. Chem. Soc.* **139**, 8752 (2017).
- [6] S. Niu, H. Huyan, Y. Liu, M. Yeung, K. Ye, L. Blankemeier, T. Orvis, D. Sarkar, D. J. Singh, R. Kapadia, and J. Ravichandran, *Adv. Mater.* **29**, 1604733 (2016).
- [7] T. Gupta, D. Ghoshal, A. Yoshimura, S. Basu, P. K. Chow, A. S. Lakhnot, J. Pandey, J. M. Warrender, H. Efstathiadis, A. Soni, E. Osei-Agyemang, G. Balasubramanian, S. Zhang, S.-F. Shi, T.-M. Lu, V. Meunier, and N. Koratkar, *Adv. Funct. Mater.* **30**, 2001387 (2020).
- [8] B. K. Mani, R. Herchig, E. Glazkova, S. Lisenkov, and I. Ponomareva, *Nanotechnology* **27**, 195705 (2016).
- [9] A. R. Chaudhuri, M. Arredondo, A. Hähnel, A. Morelli, M. Becker, M. Alexe, and I. Vrejoiu, *Phys. Rev. B* **84**, 054112 (2011).
- [10] L. Pintilie, K. Boldyreva, M. Alexe, and D. Hesse, *J. Appl. Phys.* **103**, 024101 (2008).

- [11] W. Meng, B. Saparov, F. Hong, J. Wang, D. B. Mitzi, and Y. Yan, *Chem. Mater.* **28**, 821 (2016).
- [12] N. Gross, Y.-Y. Sun, S. Perera, H. Hui, X. Wei, S. Zhang, H. Zeng, and B. A. Weinstein, *Phys. Rev. Appl.* **8**, 044014 (2017).
- [13] S. Niu, J. Milam-Guerrero, Y. Zhou, K. Ye, B. Zhao, B. C. Melot, and J. Ravichandran, *J. Mater. Res.* **33**, 4135 (2018).
- [14] W. Kohn and L. J. Sham, *Phys. Rev.* **140**, A1133 (1965).
- [15] P. Hohenberg and W. Kohn, *Phys. Rev.* **136**, B864 (1964).
- [16] G. Kresse and D. Joubert, *Phys. Rev. B* **59**, 1758 (1999).
- [17] P. E. Blöchl, *Phys. Rev. B* **50**, 17953 (1994).
- [18] G. Kresse and J. Furthmüller, *Phys. Rev. B* **54**, 11169 (1996).
- [19] J. P. Perdew, K. Burke, and M. Ernzerhof, *Phys. Rev. Lett.* **77**, 3865 (1996).
- [20] A. Togo and I. Tanaka, *Scr. Mater.* **108**, 1 (2015).
- [21] R. D. King-Smith and D. Vanderbilt, *Phys. Rev. B* **47**, 1651(R) (1993).
- [22] See Supplemental Material at <http://link.aps.org/supplemental/10.1103/PhysRevB.102.205308> for elemental mapping, tolerance factor, Raman measurements, fitting parameter, XPS measurement, and electronic band structure, as well as Refs. [23–26,32,33].
- [23] Z. Li, M. Yang, J.-S. Park, S.-H. Wei, J. J. Berry, and K. Zhu, *Chem. Mater.* **28**, 284 (2016).
- [24] S. C. Tidrow, *Ferroelectrics* **470**, 13 (2014).
- [25] N. A. Benedek and C. J. Fennie, *J. Phys. Chem. C* **117**, 13339 (2013).
- [26] J. W. Bennett, I. Grinberg, and A. M. Rappe, *Phys. Rev. B* **79**, 235115 (2009).
- [27] J. Pandey and A. Soni, *Appl. Surf. Sci.* **463**, 52 (2019).
- [28] M. N. Iliev, M. V. Abrashev, H. G. Lee, V. N. Popov, Y. Y. Sun, C. Thomsen, R. L. Meng, and C. W. Chu, *Phys. Rev. B* **57**, 2872 (1998).
- [29] T. Beechem and S. Graham, *J. Appl. Phys.* **103**, 093507 (2008).
- [30] Z. X. Shen, X. B. Wang, M. H. Kuok, and S. H. Tang, *J. Raman Spectrosc.* **29**, 379 (1998).
- [31] Y. I. Yuzyuk, R. Sakhovoy, O. Maslova, V. Shirokov, I. Zakharchenko, J. Belhadi, and M. El Marssi, *J. Appl. Phys.* **116**, 184102 (2014).
- [32] R. C. C. Leite, J. F. Scott, and T. C. Damen, *Phys. Rev. Lett.* **22**, 780 (1969).
- [33] R. C. C. Leite and J. F. Scott, *Phys. Rev. Lett.* **22**, 130 (1969).
- [34] M. Sheeraz, H. J. Kim, K.-H. Kim, J.-S. Bae, A. Y. Kim, M. Kang, J. Lee, J. Song, A. Khaliq, J. Kim, B.-G. Cho, S.-Y. Joe, J. H. Jung, J.-H. Ko, T. Y. Koo, T. W. Noh, S. Cho, S. Lee, S. M. Yang, Y.-H. Shin *et al.* *Phys. Rev. Mater.* **3**, 084405 (2019).
- [35] F. Shi, H. Dong, Q. Liu, J. Yang, S. Ren, H. Sun, and J. Xiong, *J. Mater. Sci. Mater. Electron.* **28**, 3467 (2017).
- [36] Y. Zhang, T. Shimada, T. Kitamura, and J. Wang, *J. Phys. Chem. Lett.* **8**, 5834 (2017).